NASA/TP–2006–213723

Three-Dimensional Human Bronchial-Tracheal Epithelial Tissue-Like Assemblies (TLAs) as Hosts For Severe Acute Respiratory Syndrome (SARS)-CoV Infection

SARS-CoV Infection in a 3-D HBTE Tissue-Like Assembly

*Suderman,[1,2] M.T.; McCarthy[1,2], M.; Mossell[3], E.; Watts[4], D.M.; Peters[3,4], C.J.; Shope[3],R.; and Goodwin[2], T.J.**

[1]University Space Research Association, Houston, Texas, USA 77058

[2]NASA, Johnson Space Center, Space and Life Sciences Division, Disease Modeling and Tissue Analogues Laboratory, Houston, Texas, USA 77058

[3]Departments of Microbiology and Immunology, University of Texas Medical Branch-Galveston, Galveston, Texas, USA, 77555

[4]WHO Collaborating Centers for Tropical Diseases, UTMB Center for Biodefense and Emerging Infectious Diseases, University of Texas Medical Branch-Galveston, Galveston, Texa,s USA, 77555

Correspondence*
Thomas J. Goodwin, Ph.D.
NASA Johnson Space Center,
Houston, Texas, USA 77058
Phone: 281-483-7129
FAX: 281-483-0402
thomas.j.goodwin@nasa.gov

June 2006

THE NASA STI PROGRAM OFFICE . . . IN PROFILE

Since its founding, NASA has been dedicated to the advancement of aeronautics and space science. The NASA Scientific and Technical Information (STI) Program Office plays a key part in helping NASA maintain this important role.

The NASA STI Program Office is operated by Langley Research Center, the lead center for NASA's scientific and technical information. The NASA STI Program Office provides access to the NASA STI Database, the largest collection of aeronautical and space science STI in the world. The Program Office is also NASA's institutional mechanism for disseminating the results of its research and development activities. These results are published by NASA in the NASA STI Report Series, which includes the following report types:

- TECHNICAL PUBLICATION. Reports of completed research or a major significant phase of research that present the results of NASA programs and include extensive data or theoretical analysis. Includes compilations of significant scientific and technical data and information deemed to be of continuing reference value. NASA's counterpart of peer-reviewed formal professional papers but has less stringent limitations on manuscript length and extent of graphic presentations.

- TECHNICAL MEMORANDUM. Scientific and technical findings that are preliminary or of specialized interest, e.g., quick release reports, working papers, and bibliographies that contain minimal annotation. Does not contain extensive analysis.

- CONTRACTOR REPORT. Scientific and technical findings by NASA-sponsored contractors and grantees.

- CONFERENCE PUBLICATION. Collected papers from scientific and technical conferences, symposia, seminars, or other meetings sponsored or cosponsored by NASA.

- SPECIAL PUBLICATION. Scientific, technical, or historical information from NASA programs, projects, and mission, often concerned with subjects having substantial public interest.

- TECHNICAL TRANSLATION. English-language translations of foreign scientific and technical material pertinent to NASA's mission.

Specialized services that complement the STI Program Office's diverse offerings include creating custom thesauri, building customized databases, organizing and publishing research results . . . even providing videos.

For more information about the NASA STI Program Office, see the following:

- Access the NASA STI Program Home Page at http://www.sti.nasa.gov

- E-mail your question via the Internet to help@sti.nasa.gov

- Fax your question to the NASA Access Help Desk at (301) 621-0134

- Telephone the NASA Access Help Desk at (301) 621-0390

- Write to:

NASA Access Help Desk
NASA Center for AeroSpace Information
7121 Standard
Hanover, MD 21076-1320

NASA/TP–2006–213723

Three-Dimensional Human Bronchial-Tracheal Epithelial Tissue-Like Assemblies as Hosts For Severe Acute Respiratory Syndrome-CoV Infection

SARS-CoV Infection in a 3-D HBTE Tissue-Like Assembly

*Suderman,[1,2] M.T.; McCarthy[1,2], M.; Mossell[3], E.; Watts[4], D.M.; Peters[3,4], C.J.; Shope[3],R.; and Goodwin[2], T.J.**

[1]University Space Research Association, Houston, Texas, USA 77058

[2]NASA, Johnson Space Center, Space and Life Sciences Division, Disease Modeling and Tissue Analogues Laboratory, Houston, Texas, USA 77058

[3]Departments of Microbiology and Immunology, University of Texas Medical Branch-Galveston, Galveston, Texas, USA, 77555

[4]WHO Collaborating Centers for Tropical Diseases, UTMB Center for Biodefense and Emerging Infectious Diseases, University of Texas Medical Branch-Galveston, Galveston, Texas, USA, 77555

Correspondence*
Thomas J. Goodwin, Ph.D.
NASA Johnson Space Center,
Houston, Texas, USA 77058
Phone: 281-483-7129
FAX: 281-483-0402
thomas.j.goodwin@nasa.gov

National Aeronautics and
Space Administration

Johnson Space Center
Houston, Texas 77058-3696

June 2006

Acknowledgements

The work was supported by a grant to TJG # 279-00-0308 from the Center Director's Discretionary Fund, Johnson Space Center, NASA, Houston, Texas.

The authors gratefully acknowledge Mr. Kenneth Dunner, registered electron microscopist at M.D. Anderson Research Center, HREMC, Houston, for excellent technical assistance; Dr. K.V. Holmes, University of Colorado Health Science Center, Denver, Colo., USA; Professor P.J.M. Rottier, University of Utrecht, Faculty of Veterinary Sciences, Utrecht, The Netherlands; and Dr. E. Collison, College of Veterinary Medicine, Texas A & M University, College Station, Texas, USA, for their critique and discussions.

Abstract

A three-dimensional (3-D) tissue-like assembly (TLA) of human bronchial-tracheal mesenchymal (HBTC) cells with an overlay of human bronchial epithelial (BEAS-2B) cells was constructed using a NASA Bioreactor to survey the infectivity of SARS-CoV. This TLA was inoculated with a low passage number Urbani strain of SARS-CoV. At selected intervals over a 10-day period, media and cell aliquots of the 3-D TLA were harvested for viral titer assay and for light and electron microscopy examination. All viral titer assays were negative in both BEAS-2B two-dimensional monolayer and TLA. Light microscopy immunohistochemistry demonstrated antigen–antibody reactivity with anti-SARS-CoV polyclonal antibody to spike and nuclear proteins on cell membranes and cytoplasm. Coronavirus Group 2 cross-reactivity was demonstrated by positive reaction to anti-FIPV 1 and anti-FIPV 1 and 2 antibodies. TLA examination by transmission electron microscopy indicated increasing cytoplasmic vacuolation with numerous electron-dense bodies measuring 45 to 270 nm from days 4 through 10. There was no evidence of membrane blebbing, membrane duplication, or fragmentation of organelles in the TLAs. However, progressive disruption of endoplasmic reticulum was observed throughout the cells. Antibody response to SARS-CoV specific spike and nucleocapsid glycoproteins, cross-reactivity with FIPV antibodies, and the cytoplasmic pathology suggests this HBTE TLA model is permissive to SARS-CoV infection.

Introduction

In late 2002, an acute respiratory infectious outbreak was reported from the Guangdong province of China (39 or 40 WHO; 32 Peiris et al., 2003). By early February 2003, this atypical pneumonia, now termed severe acute respiratory syndrome (SARS), had spread to adjacent Hong Kong. It subsequently spread worldwide to North America, Europe, and other Asian countries. More than 8,000 patients from over 30 countries have been exposed to SARS in the past 2 years (39 or 40 WHO).

That the causal agent to SARS was initially thought to be *Mycoplasma pneumonia*, a Chlamydia sp., or human metapneumovirus, illustrates the difficulties in the early definitive diagnosis and adequate laboratory diagnostic procedures (19 Kuiken et al., 2003). These early diagnostic efforts were limited to electron microscopy and reverse transcriptase PCR (RT-PCR) results from clinical patients. Even after the causative agent, a novel coronavirus, was identified from the results of viral genomics from laboratories worldwide, SARS was suspected of resulting from the virus in combination with other respiratory agents. The identification of virus–like particles in transmission electron microscopy cell samples from lung biopsy, pneumocytes from postmortem lung samples, and bronchoalveolar lavage samples, combined with the genomic data confirmed a previously unknown coronavirus as the potential causal agent responsible for SARS (32 Peiris et al., 2003; 4 Drosten et al., 2003; 19 Ksiazek et al., 2003; 24 Marra et al., 2003; 28 Nichols et al., 2003; and 33 Rota et al., 2003). Despite the successes of the initial studies with SARS-CoV, diagnostic and characterization efforts were limited by the non-responsiveness of the sera from convalescent patients to antibody recognition and by the early dependence on RT-PCR and transmission electron microscopy as the only reliable tools for viral identification.

The unavailability of suitable laboratory cell lines and animal models limited the early in-depth investigations of SARS-CoV. Several cell lines routinely used with respiratory viruses, such as Madin-Darby canine kidney cell (MDCK), HeLa, and LLC MK2, were determined to be unsuitable for SARS-CoV (18 Ksiazek et al., 2003). Vero E6 and NCI-H292 showed cytopathic effects after inoculation with oropharyngeal specimens collected directly from a SARS-CoV patient. A rhinovirus subsequently isolated from the NCI-H292 cell line was later determined not to have a clinical association with the SARS-CoV isolate (18 Ksiazek et al., 2003). The coronavirus-like SARS-CoV, isolated in Vero E6 cells, was identified by immunohistochemistry using cross-reactive anti-coronavirus antibodies, feline infectious peritonitis virus (FIPV), transmissible gastroenteritis virus (TGEV), and coronavirus 229E (18 Ksiazek et al., 2003). The respiratory lesions, epithelial necrosis, formation of hyaline membrane, Type 2 hyperplasia, and sancta that were experimentally reproduced within cynomolgus macaques (*Macaca fasicularis*) are analogous with clinical manifestations associated with SARS-CoV in human patients (19 Kuiken et al., 2003). Virus isolation, immunohistochemistry, transmission electron microscopy, and RT-PCR localized the SARS-CoV to alveolar epithelial cells and syncytia. When the macaques were infected with a Vero E6-cell isolate previously isolated from a SARS-CoV patient, the criteria modified by Rivers for viral diseases was met to satisfy Koch's postulates identifying this virus as the cause of disease (6 Fouchier et al., 2003).

The characterization by electron microscopy of SARS-CoV morphology from either cell culture or human biopsy material is remarkably similar. The virus can attach, enter, and uncoat the nucleocapsids within the first 30 minutes of exposure (27 Ng et al., 2003). Postinfusion entry into the cytoplasm results in the formation of large cytoplasmic vacuoles containing electron-dense particles. Electron-dense particles within cytoplasmic vacuoles are not limited to SARS-CoV or the Vero E6 cell line. Vacuoles with dense particles surrounded by a granular matrix have been associated with the human respiratory coronavirus 229E at late as 72 hours p.i. in human fetal diploid lung cells (HFDL) (31 Oshiro et al., 1971) and 62 hours p.i. in the human diploid lung cell line WI-38 (1 Becker et al., 1967). Virus particle entry into the nucleus and blebbing of the nuclear membrane has been reported in a single experiment using SARS-CoV material collected from nasal or throat swabs of SARS patients and isolated in Vero E6 cells (46 Zhang, et al., 2003).

Recent data suggest SARS-CoV-like virus or similar coronavirus sequences have been detected by RT-PCR from a number of feral animals including raccoon-dogs (*Nyctereutes proconoides*), Chinese ferret badgers (*Melogale moschata*), bats, and monkeys. The highest prevalence is seen in the Himalayan palm civet (*Paguma larvata*) (14 Guan et al., 2003). These data correlate with the elevated seropositive antibody titers noted in Chinese workers (40%) who had direct contact with live feral animals and in abattoir workers (20%), compared to 5% seen in vegetable workers (44 Yu et al., 2003) . In addition to these potential, but unlikely, laboratory animal models, recent investigations indicate domestic cats (*Felis domesticus*), ferrets (*Mustela furo*), and laboratory mice (*Mus mus*) are capable of shedding SARS-CoV virus either in the upper respiratory tract or enterically (25 Martina et al., 2003; 5 Enserink, 2003). The use of primates such as the cynomolgus macaques (*Macaca fasicularis*) as a laboratory animal model for vaccine development, pathology studies, and genomic analysis has both ethical and financial drawbacks. A laboratory model which could bridge the gap between cell culture lines and expensive animal models may be able to present the required genomic, proteomic, and physiologic data in repeatable controlled environments.

In this study, novel three-dimensional TLAs of normal human bronchial tracheal epithelial cells were engineered to investigate their suitability as a laboratory model for SARS-CoV infection and pathogenesis.

Materials and Methods

Three-Dimensional Cell Modeling. Tissue engineering NASA Bioreactors, also called rotating-wall vessels (RWVs), were used in conjunction with multicellular cocultivation to develop a unique in vitro tissue-modeling system (34 Schwarz et al., 1992). Briefly, the RWV is a horizontally rotated transparent culture vessel with zero headspace and center oxygenation. Two three-dimensional TLAs were constructed at the Cellular Environmental Toxicology and Neural Physiology (CETNEP) laboratory at Johnson Space Center, Houston, Texas, following a revised methodology (10,11,12 Goodwin et al., 1992; 1993; 1994). Commercially available HBTC cells (Cambrex BioWittaker, San Diego, CA) and BEAS-2B, a SV 40 transformed cell line from ATCC (Rockville, Md), were taken from frozen stocks and expanded using a modified tissue culture methodology (11 Goodwin et al., 1993). An in-house proprietary media GTSF-2 (HyClone, Logan, Utah, USA) was used exclusively throughout the expansion of the cell lines, and throughout the growth and maintenance of the cultures in the Bioreactor. After sufficient clonal expansion, the HBTC cells were combined with Cultispher G beads (Percell Biolytical AB Astorp, Sweeden, DG-0001-00), 100 – 200 micron macroporous gelatin microcarrier in 55.0 ml NASA Bioreactors (Synthecon, Inc., Houston, Texas, USA) for 6 days at the appropriate rotational speed. The Cultispher beads served as the initial support matrix for the attachment of the HBTC cells. The HBTC cell line has a mesenchymal cell component and an endothelial cell component that, after attachment to a single bead, will attach to additional free beads to create an expanding bead-cell matrix. On the sixth day postinfusion of HBTC and Cultispher beads in the Bioreactor, 3×10^5 BEAS-2B cells were added to the Bioreactor. The BEAS-2B cells adhered to the existing bead-cell matrix, the co-culture continued to develop until the TLAs were between 2-3 mm and the constructs were ready for exposure to the SARS-CoV strain.

Three-Dimensional Model Characterization. The three-dimensional tissue-like assembly and two-dimensional tissue culture epithelial cell monolayer were probed by immunohistochemistry to determine cellular differentiation characteristics between the two models. A three-dimensional HBTE TLA designated for histological and immunohistological staining was washed 3 times with gentle agitation in 1x PBS (Celox Laboratories Inc, St. Paul, Minn., USA) without magnesium and calcium for 5 minutes. The TLA was then transferred to a 50 ml polystyrene tube and covered with 10% buffered formalin in PBS (Electron Microscopy Service, Ft. Washington, Pa., USA) overnight at 4°C and washed 3 times in the PBS solution. The assemblies were centrifuged at less than 200x g to concentrate the bead-cell assembly after which 1 ml of 2% warm noble agar was added for additional stabilization (30 Olson et al., 1986: 20 Kung et al., 1990). Assemblies were paraffin-block embedded by standard methods, and light sections were cut at 3 to 5 mm on a Micron HM315 microtome (Walldorf, Germany). Two-dimensional tissue culture BEAS-2B monolayers were grown on sterile glass slides in sterile Petri dishes until the monolayer was 95% confluent on the slide. Slides were gently rinsed 3 times in PBS and fixed with 95% ETOH. Slides were stained with IHC antibodies on an automated immunohistochemical stainer (DAKO, Carpinteria, Calif., USA). Both 3-D and 2-D slide material were examined by a Zeiss

Axioskop (Hamburg, Germany) microscope and images captured with a Kodak DC 290 Zoom (Rochester, N.Y., USA) digital camera. Table 1 lists the antibodies used to detect cell-type-specific markers.

Virus and Infection of 3-D and 2-D Models. The Urbani strain of SARS-CoV was provided to the laboratory of C.J. Peters, M.D. at the WHO Collaborating Centers for Tropical Diseases and the UTMB Center for Biodefense and Emerging Diseases, University of Texas Medical Branch-Galveston (UTMB), Galveston, Texas. Tissue culture flasks of Vero E6 cells were grown to 85% confluency and exposed to the SARS-CoV strain for establishment of seed and progeny stock. The pre-exposure viral titer assay was determined by $TCID_{50}$ from a Vero E6 cell monolayer. A single RWV bioreactor and the HBTE co-culture were transported from Johnson Space Center to a biosafety level 3 laboratory at UTMB. The Bioreactor was set-up, and then the co-culture and 50.0 ml fresh media were added and allowed to equilibrate for 24 hours in a 37°C, 5.0% CO_2 incubator. At the same time, control T-25 tissue culture flasks of near confluent BEAS-2B 2-D monocultures were allowed to equilibrate under the same conditions. A second bioreactor with a HBTE co-culture remained at the CETNEP laboratory at Johnson Space Center as the negative control.

On day 0, a frozen aliquot of the SARS-CoV virus was rapidly thawed and added to 5.0 ml fresh GTSF-2 media to deliver an inoculum of 1.0 multiplicity of infection (MOI) at 37°C. Media were aspirated from the Bioreactor and from the 2-D tissue culture flasks, leaving just enough to ensure the cells would be covered to prevent drying. An inoculating volume of media with virions was quickly added to each tissue culture flask and to the bioreactor, which were then gently rocked to insure uniform dispersal of the inoculating media. The bioreactor and tissue culture flasks were returned to the incubator and gently rocked every 10 minutes for 60 minutes. After the 1 hour incubation, a 1.0 ml media aliquot was recovered for viral titration as was an aliquot of the 3-D TLA for light and electron microscopy respectively. The bioreactor was filled with fresh 55 ml 10% FBS GTSF-2 media and the 2-D monolayer tissue culture flasks were covered with 5 ml. of 2% FBS GTSF-2 maintenance media. This supernatant aliquot and TLA recovery was repeated at 24 hours and then at 4, 6, 8, and 10 days post-inoculation. This coincided with a 10% FBS GTSF-2 media exchange of 25-30 ml into the bioreactor. Tissue samples were either washed in 1x PBS or 0.1 M sodium cacodylate buffer pH 7.4 (Electron Microscopy Science, Fort Washington, Pa., USA), depending upon whether the tissue was processed for light or electron microscopy. Media aliquots were recovered from the 2-D BEAS-2B tissue culture flasks and from the 3-D TLAs at the same time points. Media aliquots were recovered from the Vero E6 flasks with the initial appearance of cytopathic effects (CPE) and prior to the disruption of the cell monolayer. Supernatant samples were frozen down to -70°C for viral titer assays. All media and cell aliquots remained in the biosafety hood within the Bl-3 laboratory until infectious material was rendered inert by either electron microscopy or light microscopy fixatives.

SARS-CoV $TCID_{50}$ Assay. TLA and 2-D culture supernatant samples were 10-fold serially diluted in MEM (Sigma, St. Louis, Mo., USA) supplemented with 2% FBS (Gibco, Rockville Ill., USA) to a dilution of 10^{-5}. One hundred microliters of each dilution was added to each of 4 wells of a 24-well plate, confluent with Vero E6 cells.

Plates were sealed and placed at 37°C for 1 hour. After absorption, 900 µL MEM/2% FBS was added to each well and plates were re-sealed and returned to 37°C. Four and 6 days post-inoculation plates were examined for CPE. Virus titer is expressed as Vero E6 $TCID_{50}$ PFU/ml.

Histology and Immunohistochemistry. TLAs, designated for histological and immunohistological staining, were prepared as previously described in the materials and methods. They were washed 3 times with gentle agitation in 1x PBS (Cellox Laboratories Inc, St. Paul, Minn., USA) without magnesium and calcium for 5 minutes. All unstained sections were stored at -20°C until stained with both haematoxylin and eosin (H & E), a SARS-CoV specific polyclonal antibody, or FIPV affinity purified cross- reactive antibody.

Rabbit polyclonal antibodies to putative SARS-CoV strain spike (1:400) and 3 nucleocapsid glycoproteins (1:200 – 1:1200) from Imgenex, Inc. (San Diego, Calif., USA) were used to probe day 4 through day 10 light sections. The spike protein antibody corresponded to amino acids 84-99, nucleocapsid antibody number 543 to amino acids 388- 409, nucleocapsid antibody number 544 to amino acids 396-425, nucleocapsid antibody number 548 to amino acids 399-411, and nucleocapsid antibody number 549 to amino acids 354-370 (Genebank accession no. NP_828858). The sections were deparaffinized by normal procedure. The antigen was retrieved by protein kinase or citrate and blocked with a 5% normal rabbit sera-0.05% Tween 20 solution. The primary antibody was incubated on the sections for 9 to 15 minutes, rinsed with distilled water, and a goat anti-rabbit-horseradishperoxidase second antibody (Dako Envision System, Carpinteria, Calif., USA) was applied using an automated immunohistochemical stainer (Dako Envision System, Carpinteria, Calif., USA).

A feline polyclonal antibody to feline infectious peritonitis virus (1/100, FIPV1, VMRD, Pullman, Wash., USA) was used to probe day 4 and 6 light sections. The second antibody was goat anti-feline IgA conjugated HRP, (1/100, AA125P, Serotec, Raleigh, NC, USA). A second primary affinity purified mouse anti-feline IgG to feline infectious peritonitis virus 1 and 2, (1/150 MCA2194, Serotec, Raleigh, N.C., USA), followed by either goat anti-feline IgG-HRP (AA126P, Serotec, Raleigh, N.C., USA), or F (ab′)2 rabbit anti-mouse IgG-HRP (1/150, STAR 13B, Serotec, Raleigh, N.C., USA) was used to probe day 4, 6, and 8 light sections. Slides were examined by a Zeiss Axioskop (Hamburg, Germany) microscope and images were captured with a Kodak DC 290 Zoom (Rochester, N.Y., USA) digital camera.

Transmission and Immunoelectron Microscopy. Tissue-like assembly samples were washed 3 times with 0.1 M sodium cacodylate buffer pH 7.4, then fixed in a solution of 2.5% glutaraldehyde-formaldehyde in 0.1 M sodium cacodylate buffer – 0.3 M sucrose (Sigma, St. Louis, Mo., USA) – 1% DMSO (Sigma, St. Louis, Mo., USA) pH 7.4 (Electron Microscopy Science, Fort Washington, Pa., USA) overnight at 4°C. The fixed tissue was washed 3 times in buffer, and then post-fixed stained in 0.3 M tannic acid in 0.1 M sodium cacodylate pH 7.4 for 3 hours at room temperature. The tissue samples were washed 3 times in buffer, and then fixed again in 1.0 M osmium tetroxide for 1.5 hours at room temperature. Samples were dehydrated in a series of graded ETOH, and then embedded in Spurs resin. Samples were sectioned at silver-gray

(100 – 300 µm), mounted on Ni grids, and examined under a JEOL-JEM 1010 transmission electron microscope (JEOL, USA) at 80 kV.

Results

Three-Dimensional Tissue Characterization. The results of comparative staining of two- and three-dimensional samples indicated the level of cellular differentiation was superior in the TLA constructs. Results reflected in Table 1 demonstrated greater than or equal to positive staining in human bronchial epithelial TLAs compared to positive staining in the bronchial epithelial cells in the 2-D monolayer. The cytokeratin, Factor VIII and Von Wilderbrands (VWF) antibodies detect epithelial and mesenchymal/endothelial cells, respectively (35 Shima at al, 1988; 38 Vogel et al, 1984; and 41 Woodcock et al., 1982). Villin and tubulin are cytoskeletal proteins found only in epithelial cells. ICAM-1 expression is an indicator of epithelial cell differentiation. Epithelial Membrane Antigen, ZO-1, and human mucin are specific for mucins produced by secretory human cells. Extracellular matrix component Collagen IV was also assayed to determine expression in the tissue-like structures.

Viral Assay Titer. Viral replication as manifested by titer assays was negative throughout the entire time course in both the 3-D HBTE TLA and the 2-D BEAS-2B tissue culture flask.

Light Microscopy. Three-dimensional tissue-like assemblies unexposed and exposed to SARS-CoV were sectioned and served as negative histological controls and principals. Microscopic evaluations were made over the 10 day course of the experiment. The absence of an immunological component to the TLA is indicated by hematoxylin eosin (H & E) staining, which shows an increased loss of cell mass within the matrix and on the periphery of the bead (Figs. 1, 2, 3) during the 10-day experiment. There are no infiltrating macrophages or polymorphonuclear cells responding to pro-inflammatory cytokines. The eosin stained porous material (Fig. 1) is the gelatinous matrix of the Cultispher beads, which took on a bluish tint (Fig. 2, 3). The epithelial cells are dense, cytoplasm unremarkable, and nuclei ovoid in the negative controls (Fig. 1) unlike that observed on day 4 p.i. through day 10 p.i. By day 4 p.i., the cytoplasm was granular with pinpoint multiple cytoplasmic vacuoles (Fig. 2). Atypical bronchial epithelial had irregularly distributed and condensed nuclei, prominent nucleoli, and increasing granular amphophilic cytoplasm. Zones of clearing could be noted between clusters of cells. By day 10 p.i., cells appeared less differentiated by definable cell membranes; nuclei were condensed. There was a noticeable decrease in the number of cells attached to the periphery of the beads, the greater intact cell mass being restricted to the core regions of the bead matrix.

Immunohistochemistry. The negative controls (Figs. 4, 5, 7) were probed with either the spike or the nucleocapsid peptide polyclonals. There was a consistent light background with the spike and all of the nucleocapsid polyclonals despite efforts to eliminate non-specific staining. The blue of the Mayer's counterstain, the second antibody counterstain, was readily absorbed by the gelatinous Cultispher bead. Histology sections from those samples exposed to the SARS-CoV from day 4 through day 10 inclusive were probed with the spike (Fig. 6) and nucleocapsid antibodies (Fig. 8, 9), demonstrating positive anti-SARS-CoV reaction. The reaction is confined to the cytoplasm with a discontinuous heavier reaction along some cell plasma membranes. The variable intensity of positive staining is unique to each polyclonal. Among the

nucleocapsid antibodies, polyclonal number 548 (amino acids. 399-411) required the highest titration (1/1000) to eliminate nonspecific background and over staining.

Cross-reactivity of the TLA light sectioned material to an antibody known to be reactive against this SARS-CoV strain was investigated using a feline anti-FIPV 1, a Group 2 coronavirus (Figs. 10, 11) (S. Zaki, personal communication). Light sections of day 4 p.i. that were stained at a 1/100 dilution of the primary antibody followed by a 1/100 dilution of goat anti-feline IgA-HRP demonstrated positive cross-reactivity (Fig. 11). The reactivity was the greatest in the cytoplasm of the cells in the interior of the tissue-like assembly and on the most exterior cell membranes. Unlike the granular-like cytoplasmic positive reaction observed with the anti SARS-CoV polyclonal antibody, this reaction was diffuse and uniform. There was no apparent recognition of host cell nuclear proteins or previously undetected virions attached to the cell membrane of the periphery cells.

The TLAs were further probed with a second antibody reactive to FIPV 1 and 2 (MCA2194, Serotec, Raleigh, N.C., USA) using a mouse anti-feline IgG F (ab′) 2 fragment conjugated to HRP as the chromate indicator (Figs. 12, 13). The negative control TLAs continued to demonstrate the presence of a light endogenous peroxide reaction (Fig. 12) but positive cross-reactivity to SARS-CoV could be clearly differentiated between the 2 sections (Fig. 13). Unlike the anti-FIPV 1, this antibody recognized SARS-CoV related antigen within the nucleus of day 4 through 8 cells, as well as in the cytoplasm (Fig. 13).

Electron Microscopy. Negative control and 1 hour post inoculation samples examined by transmission electron microscopy did not indicate cytopathology or virions attached to the epithelial cell membranes (Figs. 14, 15). Endoplasmic reticulum, mitochondria, nucleus, and cell membranes all appeared to be within normal parameters. Polyribosomes were evenly distributed and prominent throughout the cytoplasm. Chromatin, including both heterochromatin and euchromatin, was uniform throughout the nucleus. Epithelial cell microvilli observed on the apical aspect of the cell were intact and appeared normal.

By day 4 p.i., exposed cells were significantly different from the controls and the 1 hour exposed cells. Membranes and organelles remained intact, nuclei were uniform, not pleomorphic or displaced to 1 side of the cells. When observed, nucleoli appeared normal. Intra-nucleolus electron lucent material was only observed in the day 4 p.i. samples (Fig. 16). Microvilli were still present and did not appear to have any gross histological changes (Fig. 16). Mitochondria, when observed, were at a lower percentage per cell and swollen. Endoplasmic reticulum was disrupted rather than linear. The intra-endoplasmic compartment was noticeably distended, with the polyribosomes being less distinguishable and more widely diffused throughout the cytoplasm (Fig. 17). Translucent cytoplasmic vacuoles proximal to the cell plasma membrane did not have an electron-dense inner membrane suggestive of an exogenous origin. Likewise, cell plasma membranes did not appear to be disrupted or noticeably invaginated which could indicate postendocytosis origin of the vacuoles (Fig. 16). Double-membraned vacuoles with electron-dense material were seen throughout the cytoplasm (Figs. 16, 17); especially in those regions that previously would have been endoplasmic reticulum cysternae.

The electron-dense material within the vacuoles was pleomorphic, varying from dense aggregates located towards the periphery of the vacuoles to semi-translucent material diffused throughout the vacuole. Some electron dense aggregates within a larger vacuole appeared to have well defined margins and a core (Figs. 16, 17, 20). These defined electron dense structures ranged between 45-270 nm in diameter.

Clear areas of cell membrane disruption and necrosis were observed through the TLAs by day 6 p.i. (Figs. 18, 19). Within these areas, the junction between the cells adjacent to the beads increased from the day 4 p.i. aliquots. Polyribosomes remained evident (Fig. 18, 19), but observing mitochondria became increasing more difficult. Nuclear chromatin material appeared granular with widely diffused areas that were electron-lucent. Cytoplasmic vacuoles with the electron-dense circular material were smaller than in day 4 p.i. aliquots, 992.5 nm to 1505.3 nm, respectively. However, the vacuoles were greater in number and tended to be concentrated in those areas that had identifiable endoplasmic reticulum. Cell membrane microvilli were few in number or hard to clearly identify.

Day 8 p.i. aliquots had increased zones of cell debris within the interior of the TLAs along with an increasing number of cells detaching from the beads. Cell membranes were not observed blebbing, but they appeared to be disrupted by a lytic mechanism. The cytoplasm was almost completely devoid of polyribosomes (Fig. 20). Neither mitochondria nor endoplasmic reticulum could be observed in those cells that had large numbers of cytoplasmic vacuoles. The cytoplasmic vacuoles appeared to be orientated to the opposing poles in some cells rather than widely distributed as observed in the day 6 p.i. aliquots (Fig. 18). The electron-dense bodies with the vacuoles might have coalesced (Fig. 20), but the bodies were greater in number and more clearly defined than in previous post-infection aliquots. Translucent areas within the cytoplasm and cytoplasmic vacuoles were observed clearly for the first time (Fig. 20). Electron-translucent areas not clearly defined by a cytoplasmic membrane became increasingly evident.

By day 10 p.i., few intact cell clusters or cells remained attached to beads. The cytoplasm took on a granular appearance. This diffuse granularity was also noted in the remaining intact nuclei along with perinuclear regions of necrosis (Fig. 20). The membrane-defined cytoplasmic vacuoles had fewer electron-dense granular bodies; the remaining bodies had a more consolidated appearance (Figs. 20, 21). In some vacuoles, the granular bodies were restricted to the periphery of vacuole with the remaining vacuole volume taking on very electron-dense pleomorphic shapes. Some were horseshoe-shaped; others were shaped like commas or hyphens. Although the cytoplasmic vacuoles observed in earlier time points were scattered throughout the cytoplasm, these vacuoles either directly abutted the plasma cell membrane or were in the perimembrane space (Fig. 21). Some cells had either what could be termed “ghost” endoplasmic reticulum or, in select areas of the cytoplasm adjacent to translucent vacuoles, faint endoplasmic reticulum (Fig. 21). Large (2.4 micron) electron dense structures with an inner tubular array were observed in a number of late experiment cells. These structures had a defined architecture; however, a limiting membrane could not be observed.

Cytoplasmic inclusion material earlier described as a late maturation development (1 Becker, et al., 1967; 31 Oshiro et al., 1971) was observed throughout the day 4 p.i. through day 10 p.i. aliquots (Figs. 16, 20).

Discussion

A 3-D TLA of human bronchial epithelial cells was successfully engineered to investigate its suitability as a laboratory model for SARS-CoV infection and pathogenesis. Comparison of the degree of cellular differentiation in the TLA model to the differentiation in normal human bronchial tissue (Table 1) indicates its similarity to normal human bronchial tissue. As with Collagen IV, Mucin, and ZO-1, the level of differentiation expression is comparable between the 3-D TLA and normal tissue. A two-fold or greater level of marker expression observed in the 3-D models versus 2-D monolayers using analogous antibody dilutions supports the hypothesis of functionality differences between the two models. Analogous levels of differentiation between normal tissue and the 3-D TLA, observed with Cytokeratin 18, ZO-1, ICAM-1, and Factor VIII, supports the hypothesis that cell functionality as measured by the differentiation markers more closely resembles normal human tissue in the 3-D model than the 2-D model. Although the 3-D model does not have the histo-architecture of normal in vivo tissue, its functionality is comparable. The distal edge of the 3-D TLA has microvilli (Figs. 14, 15, 16) indicating apical polarity, essential to viral cell-cell transport via the microvilli movement along the air-liquid interface. Apical polarity is not usually seen in 2-D tissue culture systems. The model's lack of a lymphoid cell component is not a deficit with regard to studying the innate cellular response of the target cell. Measurable cellular responses to the virus are the host cell's unique innate response to the microbial pathogen. This property allows for novel investigations without the influences of an acquired response or the sequelae of adjacent cells responding to pro-inflammatory cytokines. The flexibility of the 3-D TLA to microbial infectivity and response investigations is amply demonstrated in data from Norovirus (12 Goodwin, T.J, et al., 2000), *Salmonella typimurium* (29 Nickerson, C.A. et al., 2002), Respiratory Syncytial Virus in a comparable lung model (13 Goodwin, T.J. et al., 2003; 23 Lin, Y-H, et al., 2003), West Nile Virus, N.Y. 1999 Strain, Dengue-2, New Guinea Strain, and Vesticular Stomatitus Virus, Indiana Strain experiments (unpublished data).

The lack of a recoverable viral titer and the apparent lack of observable cytopathic effects in the 2-D tissue flasks initially indicated the unsuitability of this 3-D model to SARS-CoV investigations. Earlier investigations with MDCK, HeLa and LLC MK2 cell lines, routinely used with respiratory viruses, found them to be unsatisfactory for SARS-CoV investigations (18 Ksiazek, T.G., et al., 2003). In fact, they may demonstrate some of the same properties observed in the BEAS-2B cell line. The cytopathic effects defined by rounding of cells, loss of adherence to the plastic surface of the tissue culture flask, observable granulation in the cytoplasm in the 2-D monolayers at the end of this investigation may not be characteristic of the SARS-CoV in these particular cell lines. Clinical descriptions of pulmonary pathology resulting from SARS-CoV infection include unremarkable upper respiratory tract, either unilateral or bilateral consolidation, mild pleural effusion with clear serous fluid, and pulmonary edema (37 Tse G.M-K., et al., 2004; 7 Franks T.J., et al., 2003; 3 Ding, Y., et al., 2003). Intra-alveolar exudates consisting of histocytes and acute inflammatory exudates were noted only in those cases that had concurrent secondary bacterial

infections. Atypical pneumocytes had a focal distribution and were described as multinucleated giant pneumocytes, granular amphopilic cytoplasm, and eosinophilic nucleoli. A lack of prominent upper respiratory tract pathology was noted. The morphological changes in the bronchial epithelium were denudation, loss of cilia, and squamous metaplasia (28, Nicholls, J.M., et al., 2003; 21 Lang, Z.W., 2003). Giant cell formation or synctial development was not observed in the BEAS-2B 2-D monolayers, which may indicate this cell line does respond differently to the SARS-CoV.

The lack of budding virions and infective progeny virions may be a characteristic of SARS-CoV interaction with BEAS-2B host cell genomics. The interactions of the virus with the host cell genome produces genomic RNA, antigenomic RNA, and, in some cases, subgenomic-length RNAs, all in the presence of the host cell mRNAs, tRNAs and rRNAs, resulting in infectious virions (26 Narayanan, K., 2001). In some cases, however, combining nongenomic viral RNAs and cellular RNAs results in noninfectious viruses. In this instance, the observation of cytoplasmic vacuoles (Figs. 16, 17) on day 4 p.i. indicates the S1 subunit of the coronavirus spike protein, responsible for host cell receptor recognition is apparently functional along with the S2 integral membrane portion responsible for viral and cellular membrane fusion (43 Ying, W., et al., 2004). The increasing numbers and complexity of these intra-cytoplasmic vacuoles and the electron dense particles through day 10 p.i., without the observable virion packaging, the presence of characteristic spike envelope proteins, and a definable nucleocapsid suggests post-translational modifications. These modifications either of viral or host origin allow limited packaging in the post-Golgi complex (Fig. 17) but interfere with the expression of the envelope. Thus they inhibit virion exocytosis from the cells. With certain coronavirus such as MHV, FIPV and TGEV, the membrane protein M directs the intracellular budding (17 Klumperman J., 1994). These coronaviruses bud exclusively into smooth-walled, tubulovesicular membranes located between the rough endoplasmic reticulum and the Golgi complex. However, some M proteins are transported beyond this trans-Golgi region and are held in retention. Within the coronavirus, the M protein and the spike protein S are two critical protein constituents within the envelope as it is acquired by budding at intracellular membranes. Double membrane cytoplasmic vacuoles (Figs. 16, 18, 19) were observed in the perinuclear region of the cytoplasm and within the intra-reticular endoplasmic compartment. However, viral budding was not observed from these cytoplasmic membranes. Cell loss from the beads by day 10 p.i. (Fig. 3) might be due in part to viral interference with host cell signal transduction pathways such as apoptosis and differentiation via the activator protein (AP-1), as well as from mechanical disruption by cytoplasmic vesicle (15 He, R., et al., 2003; 36 Thiel, V., et al., 2003). Why viral shedding did not take place in the course of the experiment remains to be elucidated with additional experiments into the viral genomic interactions with BEAS-2B host genome. Positive antigen-antibody response, in addition to the observations of the cytoplasmic vacuoles by transmission electron microscopy (TEM), confirms SARS-CoV entry despite the lack of traditional cytopathic effects and a recoverable viral titer.

The positive IHC staining with all antibodies probes clearly shows the presence of SARS-CoV antigen in the cytoplasm, nucleus, and cell plasma membrane of the BEAS-2B cells. Positive antibody binding was confirmed with the observed results of the negative controls and those sections stained only with the DAB-conjugated second

antibody (Figs. 4, 5, 10, 12). Sections stained with normal rabbit or normal goat serum as the first antibody did not demonstrate antibody staining (data not presented). The SARS-CoV polyclonal specific spike and nucleocapsid protein antibodies clearly recognized SARS-CoV antigens to a differing degree in the cytoplasm and along the plasma cell membrane (Figs. 6 - 9). Anti-SARS-CoV spike antibody staining at day 4 p.i. was restricted to the cytoplasm with no nuclear involvement. The intensity of staining even at a 1/100 dilution was light and diffuse; however, the cytoplasm did have a granular appearance throughout the course of the experiment (Fig. 6). Anti-nucleocapsid protein # 543 (amino acid 388-409) could be differentiated from # 548 (amino acid 399-411) and # 549 (amino acid. 354-370) by the level of intensity (Fig. 9), recognition of antigen along the plasma cell membranes (Figs. 8, 9), and increased antigen recognition within the nucleus (Fig. 9). Coronavirus nucleoprotein involvement in the host cell nucleolus has been reported with avian bronchitis (16 Hiscox, J.A., 2001), TGEV (42 Wurm, T., 2001), and MHV (22 Li, H-P., 1997). SARS-CoV cross-reactivity with monoclonal anti-feline infectious peritonitis virus 1 (FIPV-1) is similar to the earlier cross-reactivity observations involving the Urbani strain (18 Ksiazek, T.G., et al., 2003: Zaki, S., personal communication 2003) and a second anti-feline FIPV 1 and 2 antibody, which had never been tested against SARS-CoV, was noted. Both anti-FIPVs recognized SARS-CoV antigen within the host cell nucleus, however, the second FIPV had a higher affinity for the antigen as seen by the heavier staining reaction. The intra-nuclear antigen recognition by the FIPV antibodies may be similar to the observations with transmissible gastroenteritis virus (TGEV) and MHV localizing in the nucleolus while the host cells are undergoing cell division (42 Wurm, T., et al., 2001). This involvement plays a determining role in the disruption of the cell cycle in interphase, thereby inhibiting cytokinesis in those cells infected with avian coronavirus infectious bronchitis virus (IBV) (2 Chen et al., 2002). Nucleoli were observed in a percentage of cells in those sections stained with the anti-FIPV antibodies, generally late into the experiment (Fig. 13). SARS-CoV antigen was present in the nucleus, but whether it had an active role in the disruption of the cell cycle in the TLA remains speculative.

Examination of ultra-thin sections by transmission electron microscopy indicated similar and dissimilar observations with other coronavirus investigations. Cytoplasmic vacuole development and proximal membrane vacuolation in negative controls and 1 hour sections (Figs. 14, 15) differ from the observations of SARS-CoV in Vero E6 2-D tissue cultures (46 Zhang, et al., 2003; 27 Ng, M.L. et al., 2003). Vacuolation at the cell plasma membrane, well defined electron dense cytoplasmic vacuoles with electron dense particles budding from the intra-cytoplasmic membrane into the vacuole lumen, were characteristics observed in the 3-D TLA. Comparison of the negative controls to exposed sections from day 4 p.i. through day 10 p.i. confirms the loss of discernable endoplasmic reticulum (Figs. 16, 18, 19, 21), swelling and loss of mitochondria, and alterations in the distribution of chromatin (Figs. 16, 18). In few instances, small translucent vacuoles were seen just below the plasma cell membrane at 1 hour (Fig. 15). Sub-membrane vacuoles observed on day 4 p.i. would be more suggestive of cytoplasmic vacuoles with assembled virions preparing to bud from the cell membrane than newly acquired virions (Fig. 16).

Multiple cytoplasmic vacuoles with electron-dense particles were clearly visible from day 4 p.i. through day 10 p.i. The vacuoles were pleomorphic, and those perinuclear did not appear to be smaller or more condensed than those distal to the nucleus at day 4 p.i. (Fig. 16). At day 4 p.i. some vacuoles appeared to be in the intra-endoplasmic reticulum compartment (Fig. 17). The vacuole's double membrane could be better observed at higher magnification at day 4 p.i. The electron dense particles were generally clustered near one edge but not in direct contact with the vacuole membrane. Particles ranged from 45 to 270 nm in diameter, larger than the previously described SARS-CoV maturation particles from WI-38, human fetal diploid lung cells, or Vero E6 cell lines (1 Becker et al., 1967; 31 Oshiro, et al., 1971; 27 Ng, et al., 2003; 46 Zhang, et al., 2003).

Observations with either coronavirus 229E or SARS-CoV regarding cytoplasmic vacuoles, electron dense granular particles, and morphological changes within the host cell suggest the human bronchial epithelial TLA is a suitable model for investigations into coronavirus infectivity and pathogenesis. The TLA remained viable in culture three times longer than in 2-D tissue cultures. It is engineered with normal human cells, the response to the microbial agent is of human cell origin, and it is repeatable using the same cell lines and potentially the same cell passage number. Positive antigen-antibody response, in addition to the TEM observations, confirms SARS-CoV entry into the cells despite the lack of traditional cytopathic effects and a recoverable viral titer. Although the significance of not detecting progeny virions cannot be overlooked, the comprehension of the viral-host cell genomic interactions may be the greater consideration to potential vaccine development and the characterization of coronavirus influenced histopathology.

References

1. Becker, W.B., McIntosh, K., Dees J.H., & Chanock, R.M. (1967). Morphogenesis of avian infectious bronchitis virus and a related human virus (strain 229E). J Virol **1**, 1019-1027.
2. Chen, H., Wurm, T., Britton, P., Brooks, G., Hiscox, J.A. (2002). Interaction of the coronavirus nucleoprotein with nucleolar antigens and the host cell. J Virol **76** 5233-5250.
3. Ding, Y., Wang, H., Shen, H., Li, Z., Geng, J., Han, H., et al. (2003). The clinical pathology of severe acute respiratory syndrome (SARS): a report from China. J Pathol **200**, 282-289.
4. Drosten, C., Gunther, S., Preiser, W., et al. (2003). Identification of a novel coronavirus in patients with severe acute respiratory syndrome. N Engl J Med **348**, 1967-1976.
5. Enserink, M., (2003). SARS researchers report new animal models. *Science* **302**, 213.
6. Fouchier, R.A., Kuiken T., Schutten, M., van Amerongen, G., et al. (2003). Aeitiology: Koch's postulates fulfilled for SARS virus. *Nature* **423**, 240.
7. Franks, T.J., Chong, P-E-K., Chui, P., Galvin, J.R., Lourens, R.A., Reid, A.H., Selebs, El., McEvoy, P.L., Hayden, D.L., Fukuoka, J., Taubenberger, J.K., and Travis, W.D. (2003) Lung pathology of severe acute respiratory syndrome (SARS): a study of 8 autopsy cases from Singapore. Human Pathol. **34** (8) 743-748.
8. Haake A.R., Lane H.T. (1989). Retention of differentiated characteristics in human fetal keratinocytes. In Vitro **25**,592–600.
9. Goodwin T.J., Jessup J.M., Wolf DA. (1992). Morphologic differentiation of colon carcinoma cell lines HT-29 and HT-29KM in rotating wall vessels. In Vitro 28A, 47–60.
10. Goodwin, T.J., Schroeder, W.F., Wolf, D.A., Moyer, M.P. (1993). Coculture of Normal Human Small Intestine Cells in a Rotating-Wall Vessel Culture System. *Proceedings of the Society for Experimental Biology and Medicine* Vol. 202.
11. Goodwin, T.J. *et al.* (1994). Multicellular three-dimensional living mammalian tissue. U. S. Patent 5,308,764, uspto.gov.
12. Goodwin, T.J. *et al*. (2000) "Pathogen Propagation in Cultured Three-Dimensional Tissue Masses", U.S. Patent, 6,117,674
13. Goodwin, T.J., Deatly, A., Suderman, M.T., Lin, Y-H., Chen, W., Gupta, C.K., Randolph, V.B., Udem, S.A. (2003). Three-dimensional engineered high fidelity normal human lung tissue-like assemblies as targets for human respiratory virus infection. Amer Soc Virol Annual Meeting, Abstr. **W20-09.**

14. Guan, Y., Zheng, B. J., He, Y. Q., Liu, X. L., et al. (2003). Isolation and characterization of viruses related to the SARS coronavirus from animals in southern China. *Sciencexpress* **10.1126**-Science.1087139, 1-10.

15. He, R., Leeson A., Andonov, A., Li, Y., Bastien, N., Cao, J., Osiowy, C., Dobie, F., Cutts, T., Ballantine, M., Li, X. (2003). Activation of Ap-1 signal transduction pathway by SARS coronavirus nucleocapsid protein. Biochem Biophy. Res Comm. **311**, 870-876.

16. Hiscox, J.A., Worm, T., Wilson, L., Britton, P., Cavanagh, D., Brooks, G. (2001)**.** The coronavirus infectious bronchitis virus nucleoprotein localizes to the nucleolus. J Virol **75**, 506-512.

17. Klumperman, J., Locker, J.K., Meijer, A., Horzinek, M.C., Geuze, H.J., Rottier, P.J.M. (1994). Coronavirus M proteins accumulate in the golgi complex beyond the site of virion budding. J Virol **68**, 6523-6534.

18. Ksiazek, T. G., Erdman, D., Goldsmith, C. S., et al. (2003). A novel coronavirus associated with severe acute respiratory syndrome. *N Engl J Med* **348**, 1953-1966.

19. Kuiken, T., Fouchier, R. A. M., Schutten, M., Rimmelzwaan, G. F., et al. (2003). Newly discovered coronavirus as the primary cause of severe acute respiratory syndrome. *Lancet* **362**, 263-270.

20. Kung, I.T., Chan, S.K., Lo, E.S. (1990). Application of the immunoperoxidase technique to cell block preparations from fine needle aspirates. Acta. Cytol **34**,297-303.

21. Lang, Z. W., Zhang, L.J., Zhang, S.J., Meng, X., et al. (2003). A clinicopathological study of three cases of severe acute respiratory syndrome (SARS). *Pathology* **35(6)**, 526-531.

22. Li, H-P., Zhang, X., Duncan, R., Comai, L., Lai, M.M. (1997). Heterogenous nuclear ribonucleoprotein A1 binds to the transcription-regulatory region of mouse hepatitis virus. Proc. Natl. Acad. Sci. USA. **94**, 9544-9549.

23. Lin, Y-H., Deatly, A.M., Chen, W., Goodwin, T.J., Suderman, M.T., Randolph, V.B., Udem, S.A. (2003). Differentiating replication efficiencies of respiratory syncytial virus using a 3-D engineered normal human lung cell culture model. Amer Soc Virol annual meeting, Abstr. **W20-10.**

24. Marra, M. A., Jones, S. J., Astell, C. R., Holt, R. A., et al. (2003). The genome sequence of the SARS-associated coronavirus. *Science* **300**, 1399-1404.

25. Martina, B.E, Haagmans, B.L., Kuiken, T., Fouchier, R.A., et al. (2003). SARS virus infection of cats and ferrets. *Nature* **425**, 915.

26. Narayanan, K. and Makino, S. (2001). Cooperation of an RNA packaging signal and a viral envelope protein in coronavirus RNA packaging. J Virol. **75**, 9059-9067.

27. Ng, M.L., Tan, S.H., See, E.E., Ooi, E.E., Ling, A.E. (2003). Early events of SARS coronavirus infection of Vero cells. *J of Med Virol* **71**, 323-331.

28. Nicholls, J. M., Poon, L.L., Lee, K.C., Ng, W.F., et al. (2003)**.** Lung pathology of fatal severe acute respiratory syndrome. *Lancet* **361**, 1773-1778.

29. Nickerson,C.A., Goodwin, T.J., Terlonge, J., Ott, C.M., Buchanan, K.L., Uicker, W.B., Emami, K., Cedor, C. L., Ramamurthy, R., Clarke, N.S., Hammond, T., Pierson, D.L. (2001). Three-dimensional tissue assemblies: novel models for the study of Salmonella pathogensis. Infec Immun **69,** 7106-7120.

30. Olson, N.J., Gogel, H.K., Williams, W.L., Mettler, F.A.J. (1986). Processing of aspiration cytology samples. An alternative method. Acta Cytol **30**,409-412.

31. Oshiro, L.S., Schieble, J.H., Lennette, E.H. (1971). Electron microscopic studies of coronavirus. *J Gen Virol* **12**, 161-168.

32. Peiris, J.S., Lai, S.T., Poon, L.L., et al. (2003). Coronavirus as a possible cause of severe acute respiratory syndrome. *Lancet* **361**, 1319-1325.

33. Rota, P.A., Oberste, M. S., Monroe, S.S., et al. (2003). Characterization of a novel coronavirus associated with severe acute respiratory syndrome. *Science* **300**, 1394-1399.

34. Schwarz, R.P., Goodwin, T.J., Wolf, D.A. (1992). Cell culture for three dimensional modeling in rotating-wall vessels: An application of simulated microgravity. J Tiss Cult Meth **14**, 51–58.

35. **S**hima, M., Yoshioka, A., Nakai, H., Tanaka, I., Fujiwara, T., Terada S., Imai, S., Fukui, H. (1988). Factor VIII polypeptide specificity of monoclonal anti-factor VIII antibodies. Br J Haematology **70** 63–69.

36. Thiel, V., Ivanov, K.A., Putics, A., Hertzig, T., et al. (2003). Mechanisms and enzymes involved in SARS coronavirus genome expression. *J of Gen Virol* **84**, 2305-2315.

37. Tse, G. M-K., To, K-F., Chan P.K-S., Lo, A.W. I., Ng, K-C., Wu, A., Lee, N., Wong, H-C., Mak, S-M., Chan, M-F., Hui, D.S.C., Sung J. J-Y., Ng, H-K. (2004)**.** Pulmonary pathological features in coronavirus associated severe acute respiratory syndrome (SARS). *J Clin Pathol* **57**, 260-265.

38. Vogel, A.M., Gown, A.M. Monoclonal antibodies to intermediate filament proteins. In: Shay JW, Ed. Cell and Muscle Motility. New York: Plenum Publishing, Vol **5**: pp379–402, 1984.

39. WHO. (2003). Severe acute respiratory syndrome (SARS)- multi-country outbreak. World Health Organization Update **43**.

40. WHO. (2003). Severe acute respiratory syndrome (SARS)-multicountries outbreak update. World Health Organization **73.**

41. Woodcock-Mitchell, J., Eichman, R., Nelson, W.G., Sun T. (1982)**.** Immunolocalization of keratin polypeptides in human epidermis using monoclonal antibodies. J Cell Biol 95,580–588.

42. Wurm, T., Chen, H., Hodgson, T., Britton, P., Brooks, G., Hiscox, J.A. (2001). Localization to the nucleolus is a common feature of coronavirus nucleoproteins, and the protein may disrupt host cell division. J Virol **75**, 9345-9356.

43. Ying, W., Hao, Y., Zhang, Y., Peng, W., Qin, E., Cai, Y., Wei, K., et al. (2204). Proteomic analysis on structural proteins of severe acute respiratory sundrome coronavirus. Proteomics **4**, 492-504.

44. Yu, D., Li, H., Xu, R., He, J. et al. (2003). Prevalence of IgG antibody to SARS- associated coronavirus in animal traders- Guangdong Province, China, 2003. MMWR, CDC **52**, 986-987.

45. Zaki, S. personal communication, CDC, Atlanta Georgia.

46. Zang, Q.F., Cui, J.M., Huang, X.J., Lin W. et al. (2003). Morphology and morphogenesis of severe acute respiratory syndrome (SARS)-associated virus. Acta Biochimica et Biophysica Sinica 35, 587-591.

Table 1

Tissue Characterization Stains	Normal Hu Lung Tissue	3-D HBTE TLA	2-D BEAS-2B Cells
ZO-1	3+	4+	1+
Epithelial Membrane Ag. (EMA)	4+	2+	0
ICAM-1 (CD54)	3+	4+	0
Villin	2+	3+	1+
Tubulin	3+	4+	1+
Cytokeratin 18	3+	4+	1+
VWF/Factor VIII	4+	3+	1+
Collagen IV	4+	4+	2+
Hu Mucin	4+	4+	1+

Comparison of normal human bronchial tracheal tissue differentiation to 3-D TLA and 2-D tissue culture monolayer indicated by IHC staining. ND = Not Done

Figures

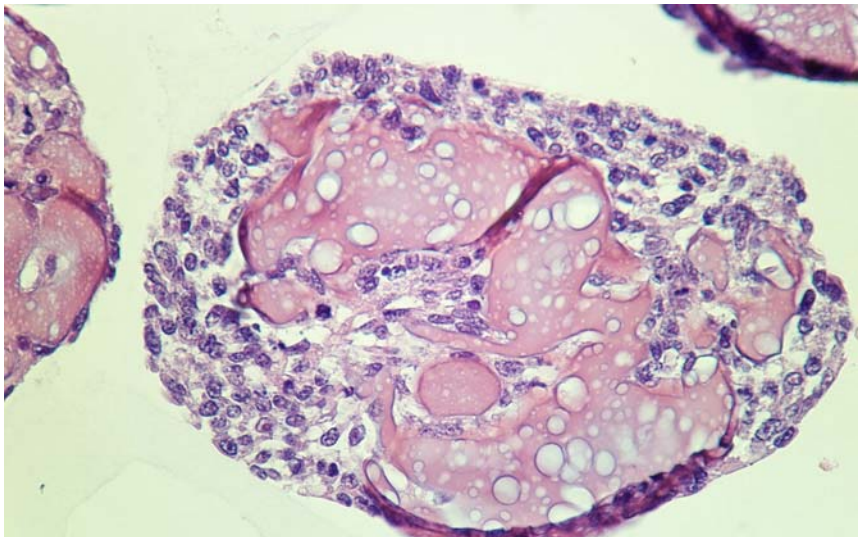

Figure 1. Unexposed HBTE control. Cells are normal, cytoplasm is agranular, nuclei are ovoid, and nucleoli have taken up the eosin stain. H&E 400x

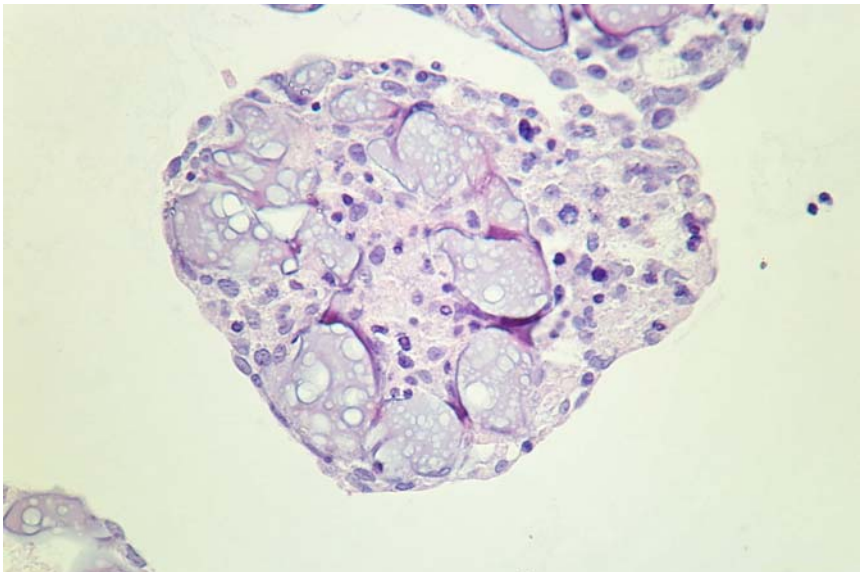

Figure 2. HBTE SARS-CoV, day 4 p.i. cells show little histopathology, cytoplasm has granular appearance. H&E 400x

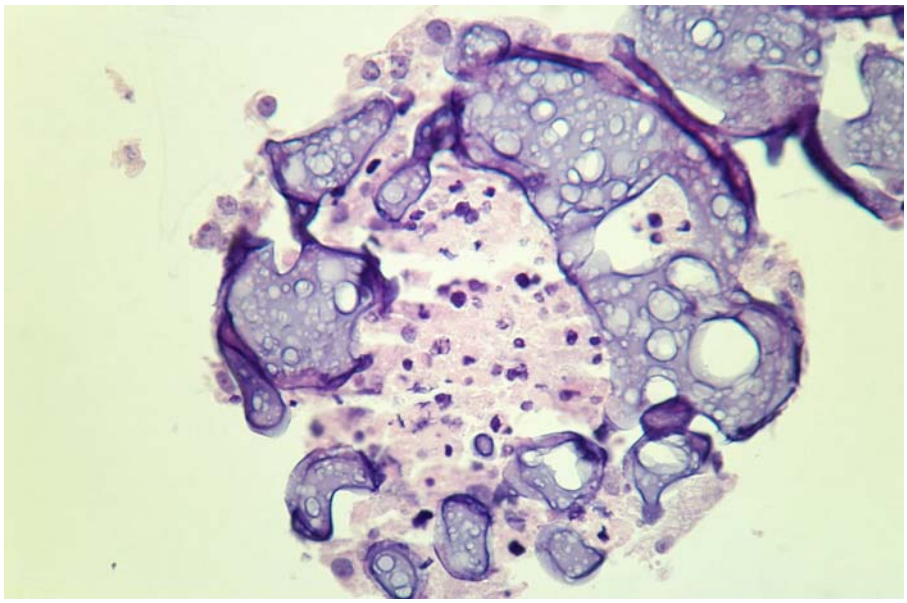

Figure 3. HBTE SARS-CoV. Day 10 p.i. cells remaining are in the core of the gel matrix. Cytoplasm has pale eosin blush, nuclei are pleomorphic. Proportionally large nuclei, but no multinucleated cells or syncytia. H&E 400x

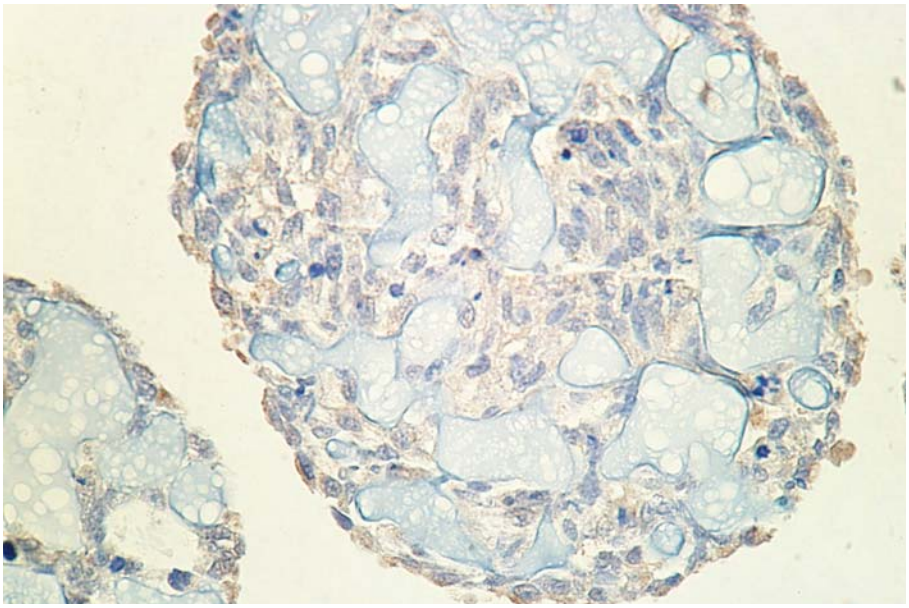

Figure 4. HBTE Negative Control SARS-CoV specific polyclonal spike antibody probed against a day 4 p.i. matched unexposed 3-D TLA. Uniform light endogenous peroxide reaction on the peripheral cells. Azure stain from the Mayer's counterstain. 400x

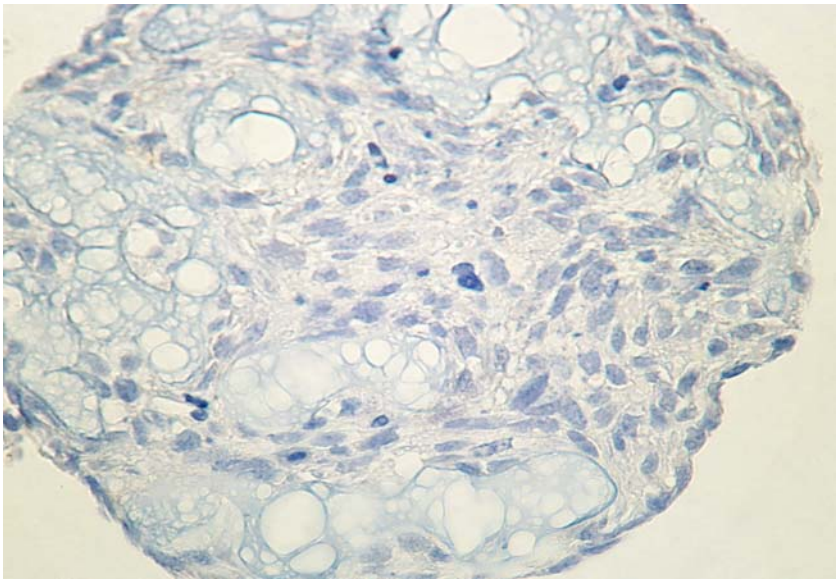

Figure 5. HBTE Negative Control. SARS-CoV specific polyclonal anti-nucleocapsid protein # 543 probed against a day 4 p.i. matched unexposed 3-D TLA. Azure stain from the Mayer's counterstain. 400x

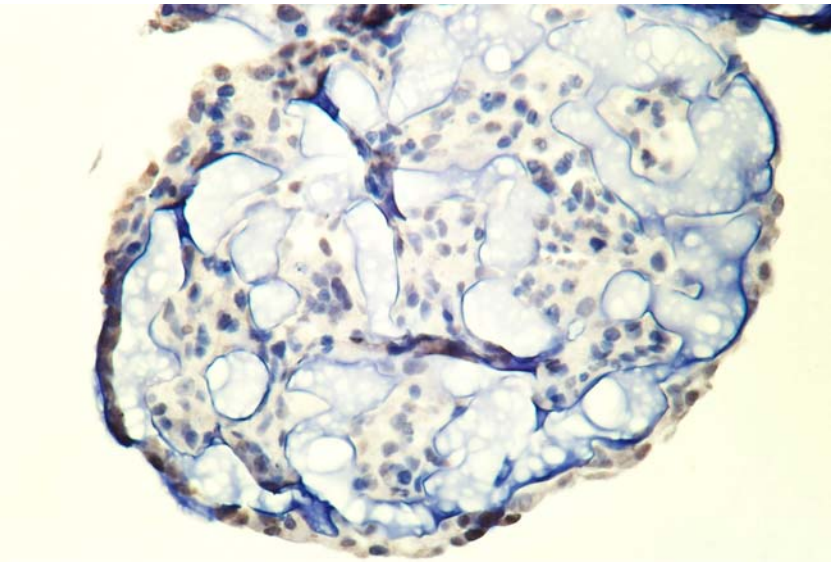

Figure 6. HBTE SARS-CoV specific polyclonal anti-spike antibody. Day 4 p.i. Uniform light stain in the cytoplasm, especially on the peripheral cells. 400x

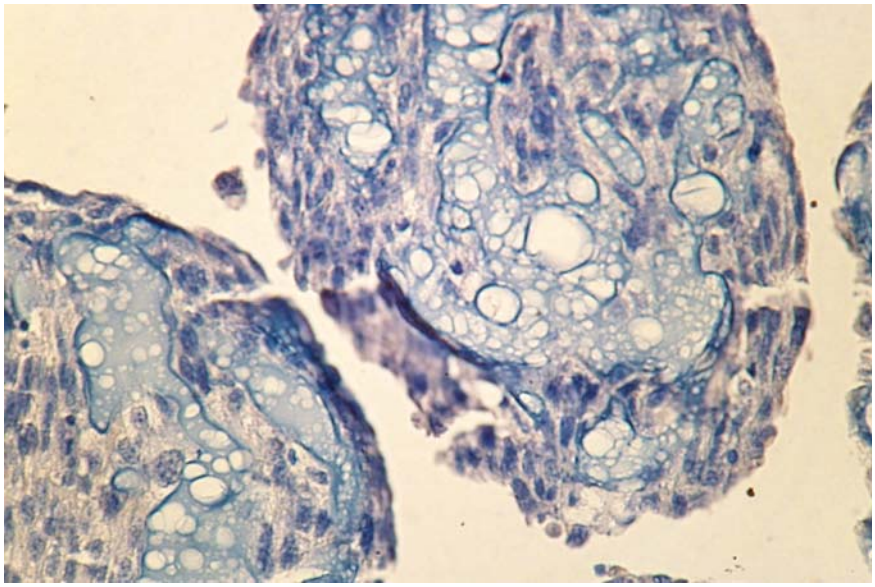

Figure 7. HBTE. Negative Control SARS-CoV coronavirus specific anti-nucleocapsid polyclonal # 543 probed against a day 4 p.i. matched unexposed 3-D TLA. 400x

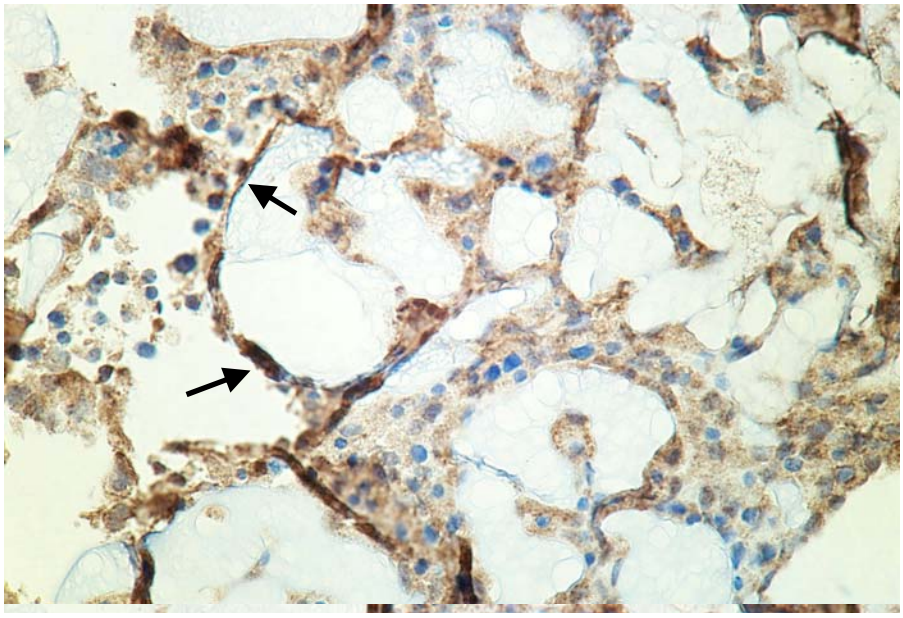

Figure 8. HBTE. SARS-CoV specific polyclonal nucleocapsid protein antibody # 548. Greater staining intensity along cell membrane outlining the interface of the Cultispher bead and the basal border of the HBTE cell (arrows). Cytoplasm has granular appearance, some antigen-antibody reaction in the nuclei. on day 4 p.i. 400x

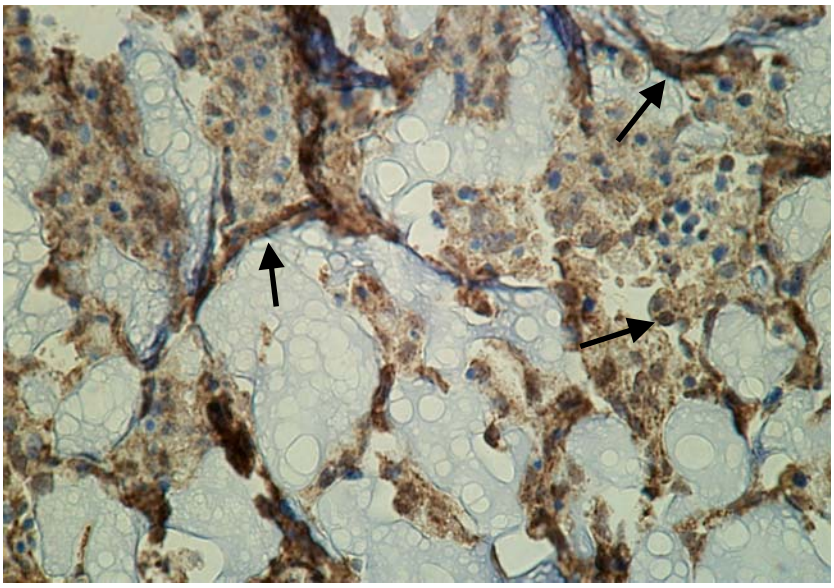

Figure 9. HBTE SARS-CoV specific polyclonal nucleocapsid protein # 549. Greater staining intensity along the cell membrane (small arrows). Cytoplasm has less reaction than the cell plasma membrane day; distinct granular particles observed in the cytoplasm, nuclei are not uniformly stained. Day 4 p.i. 400x

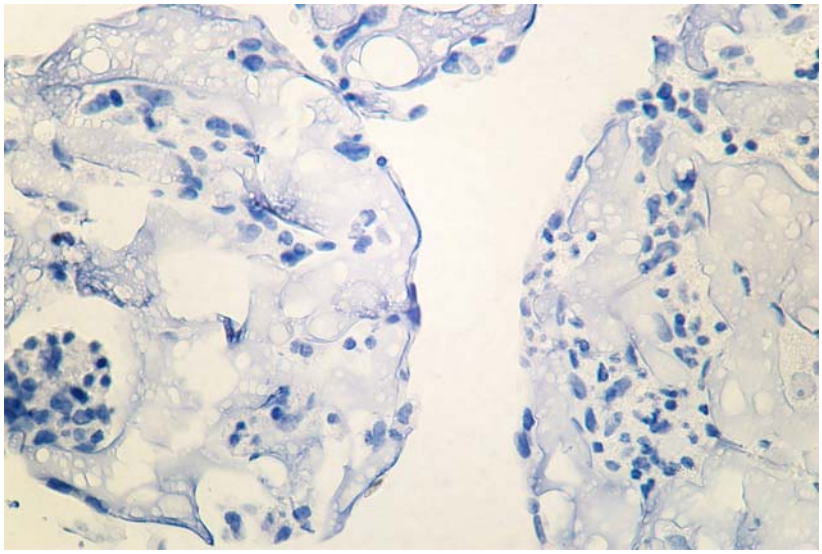

Figure 10. HBTE. Negative Control Cross-reactivity of anti-FIPV-1 antibody to SARS-CoV. A day 4 p.i. matched unexposed 3-D TLA probed with anti-FIPV-1 Ab (1/100). No observable reaction. Azure stain from the Mayer's counterstain. 400x

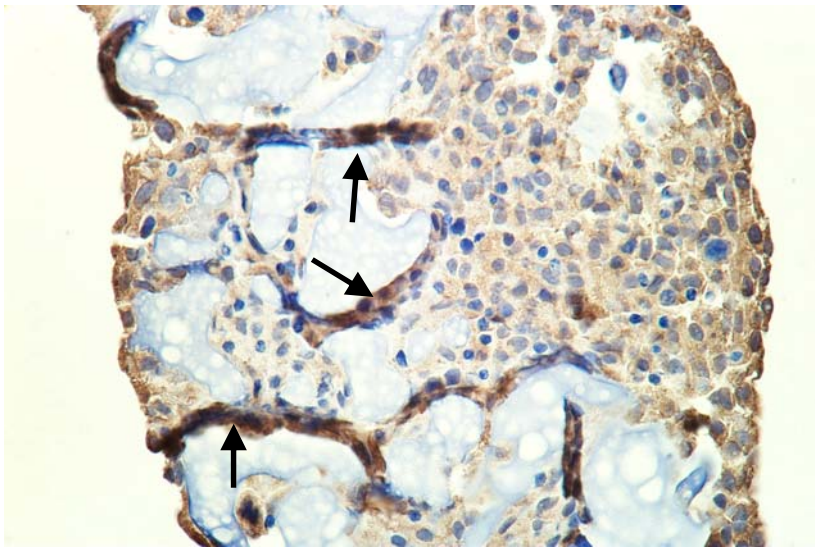

Figure 11. HBTE. Cross-reactivity of anti-FIPV-1 antibody to SARS-CoV. A day 4 p.i. exposed 3-D TLA probed with anti-FIPV 1 Ab (1/100). Cross-reactivity in the cytoplasm of peripheral and interior cells. Cytoplasm has granular appearance; few nuclei appear to have taken up the stain. 400x

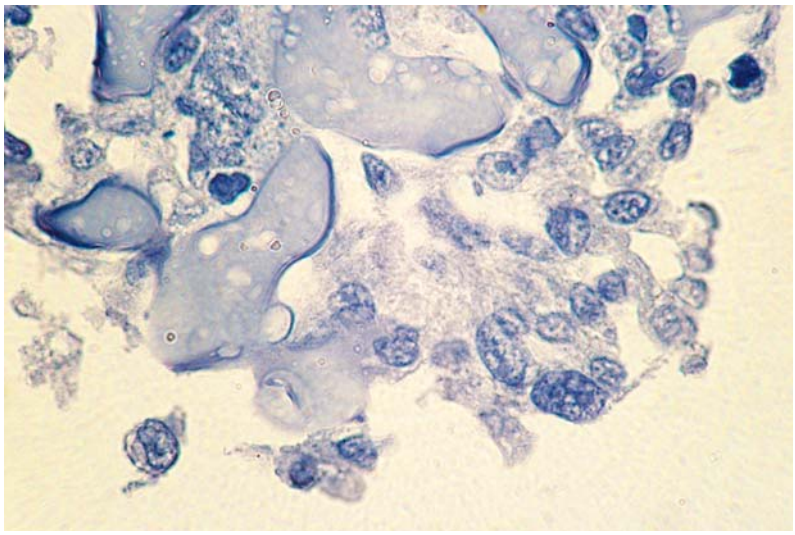

Figure 12. HBTE. Negative Control. Cross-reactivity of anti-FIPV 1 and 2 Ab to SARS-CoV. A day 6 p.i. matched unexposed 3-D TLA probe with anti-FIPV 1 & 2 (1/100) and counterstained with F (ab′) 2 (1/150). Light brown stained areas are the result of endogenous peroxide reactions. Azure stain from the Mayer's counterstain. 1000x.

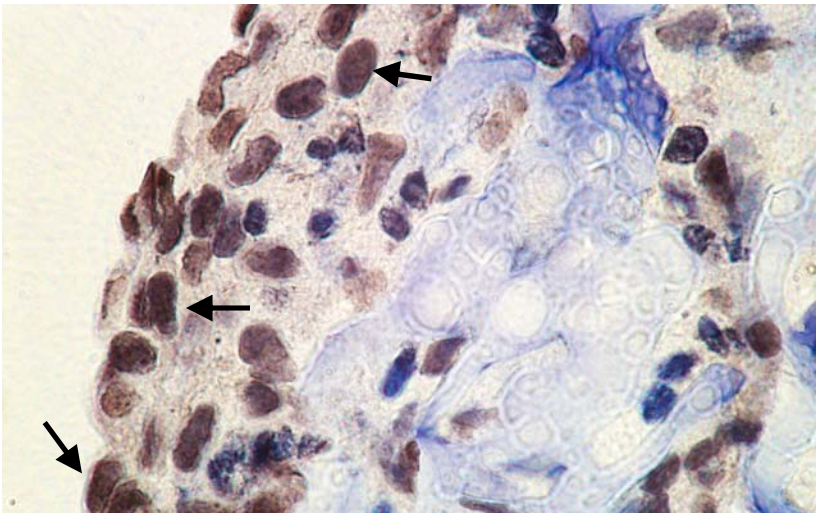

Figure 13. HBTE. SARS-CoV exposed day 6 p.i. TLA at a 1/100 dilution probed with anti-FIPV 1 & 2. Positive cross–reaction with SARS-CoV. Staining evident on the cell plasma membranes of peripheral cells and cytoplasm of interior cells. Cytoplasm has granular appearance and nuclei are heavily stained. 1000x

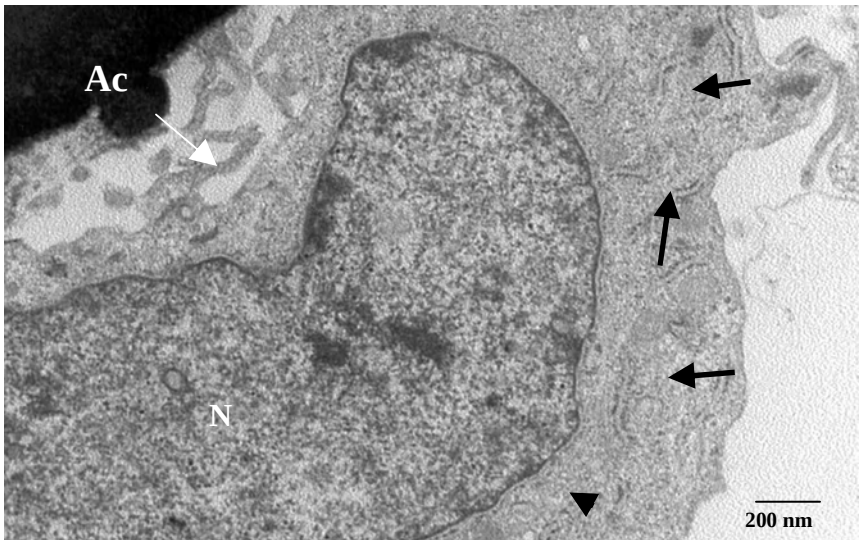

Figure 14. HBTE. TEM of a negative control TLA section. The nucleus (N), endoplasmic reticulum (arrows) and mitochondria (arrow heads) appear within normal parameters. The differentiation characteristic, cellular polarity, is indicated by the apical microvilli (Ac). Original magnification was used, 12000x.

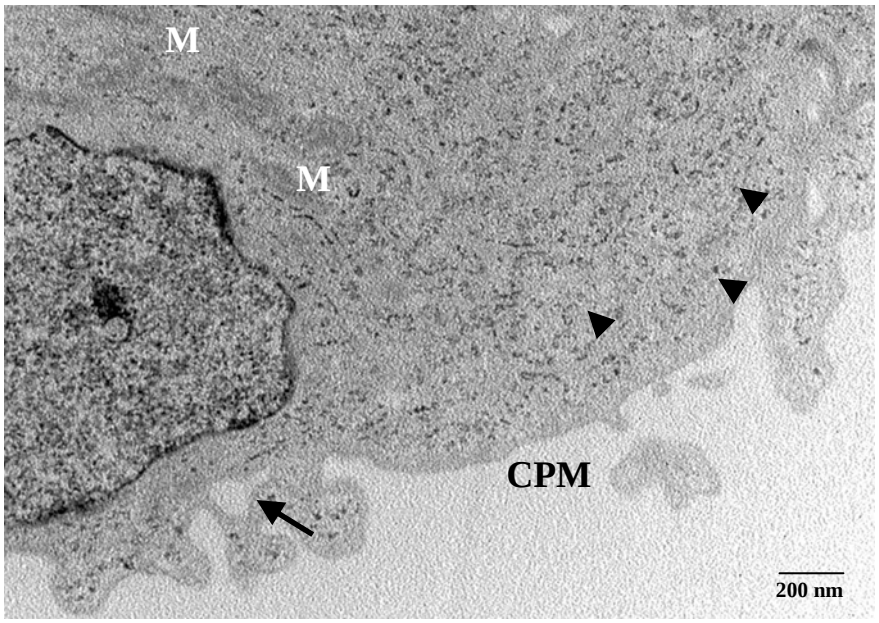

Figure 15. HBTE. TEM of exposed TLA at 1 hour p.i. Mitochondria are visible, not swollen; endoplasmic reticulum (arrowheads) are clearly defined distal to the nucleus; and the nucleus appears normal. Single intracellular translucent vacuole (arrow) are near the cell plasma membrane. Neither electron-dense-particles nor vacuolar membrane is noticeable. Original magnification was used, 12000x.

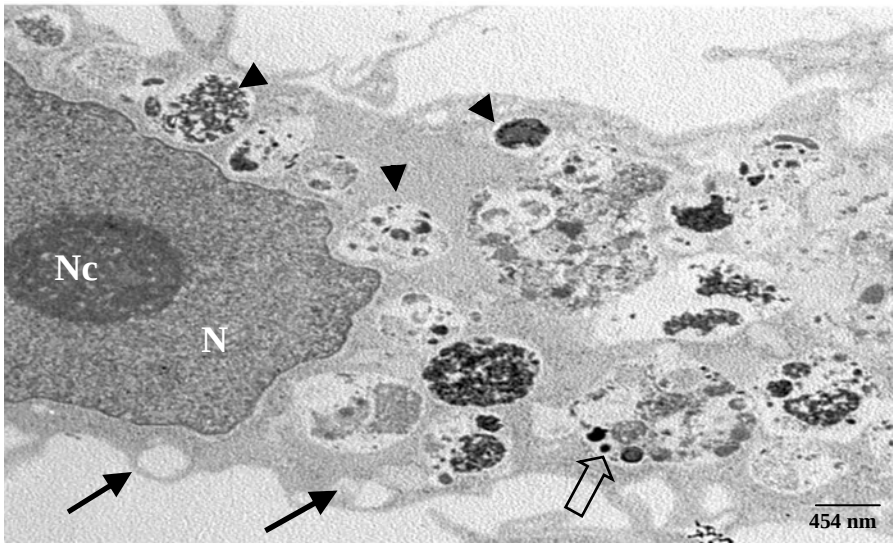

Figure 16. HBTE TEM of exposed TLA at day 4 p.i. Nucleus (N) and nucleolus (Nc) are intact; nuclear chromatin is uniformly dense. Nucleolus has pinpoint translucent areas within its border. There were multiple cytoplasmic vacuoles (arrowheads) with electron-dense material. Sub-membrane vacuoles (arrows) are translucent without clearly defined cytoplasmic membrane. Large cytoplasmic vacuole (large open arrow) contains multiple electron-dense granules, and defined inner compartments with granular structures and is bordered by defined translucent zone. Original magnification was used, 7500x.

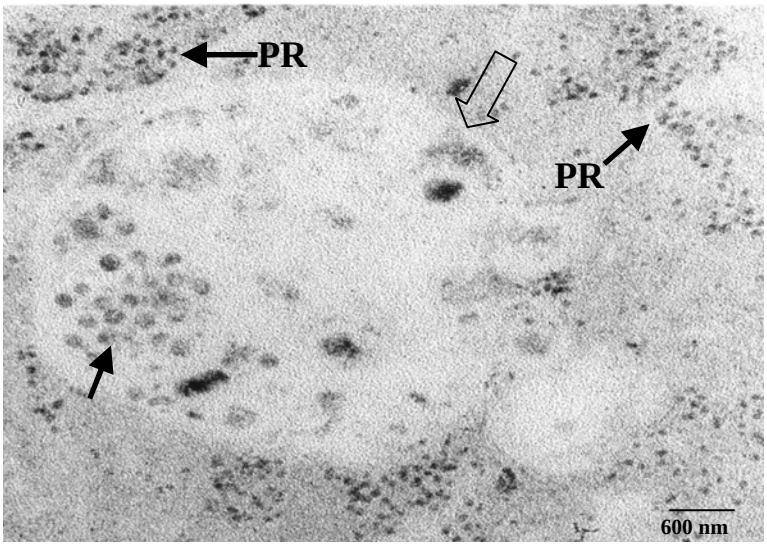

Figure 17. HBTE high magnification TEM of exposed TLA at day 4 p.i. Cytoplasmic vacuole separated from cell cytoplasm by translucent membrane (large open arrow) with well-defined electron-dense granular particles (arrow). Vacuole is positioned in the intra-endoplasmic reticulum compartment. Original magnification was used, 60000x.

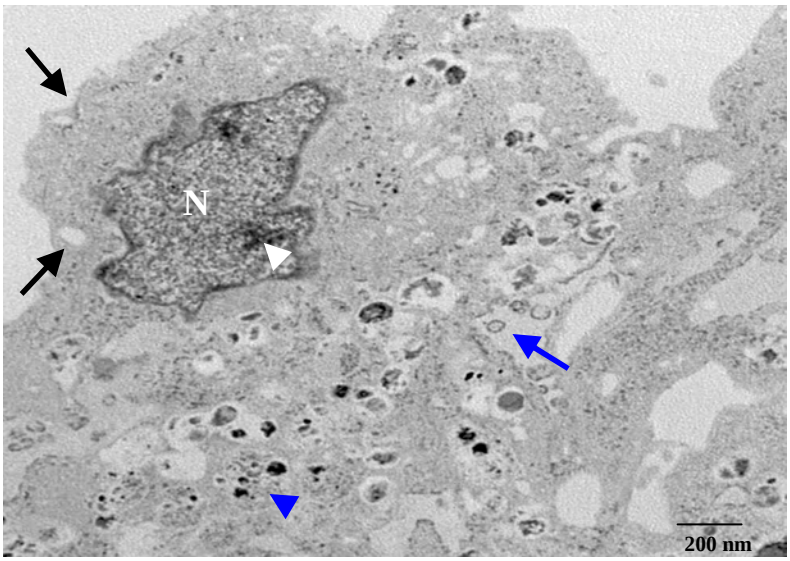

Figure 18. HBTE TEM of exposed TLA at day 6 p.i. The nucleus (N) is pleomorphic, shifted towards the edge of the cell, has granular chromatin material with several electron dense particles within the nuclear membrane (arrowheads). The cytoplasmic vacuoles with electron dense granules are compact, defined by translucent border (small arrow). Translucent cytoplasmic vacuoles are pronounced (arrows). Neither mitochondria, endoplasmic reticulum, nor polyribosomes are noticeable. Original magnification was used, 7500x.

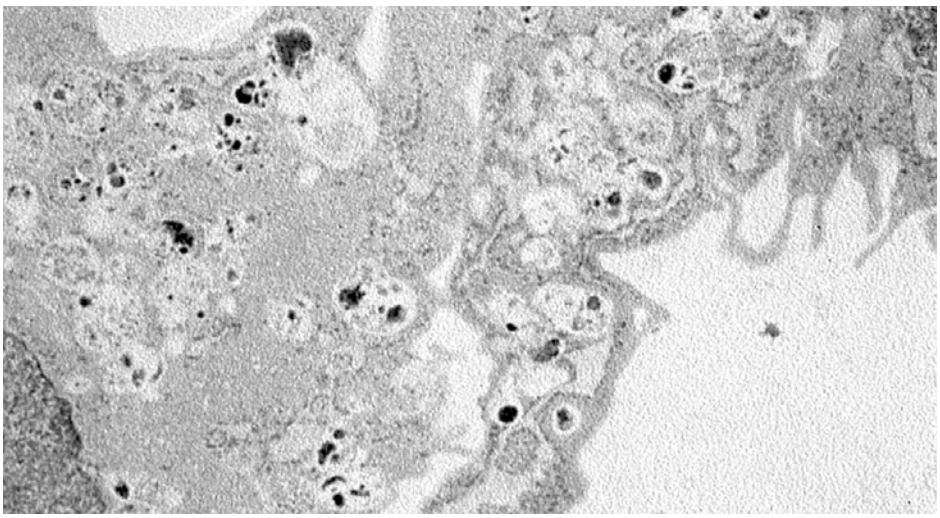

Figure 19. HBTE TEM of exposed TLA at day 8 p.i. Three cells are in close proximity to each other (labeled 1,2,3). Cell 1 has intact nucleus (N) with numerous perinuclear cytoplasmic vacuoles (arrowhead) containing electron-dense granules. Cell 2 has numerous cytoplasmic vacuoles containing pleomorphic electron dense granules (arrows). Cell 3 has distinctive polyribosomes and apical microvilli (Ac). Original magnification was used, 7500x.

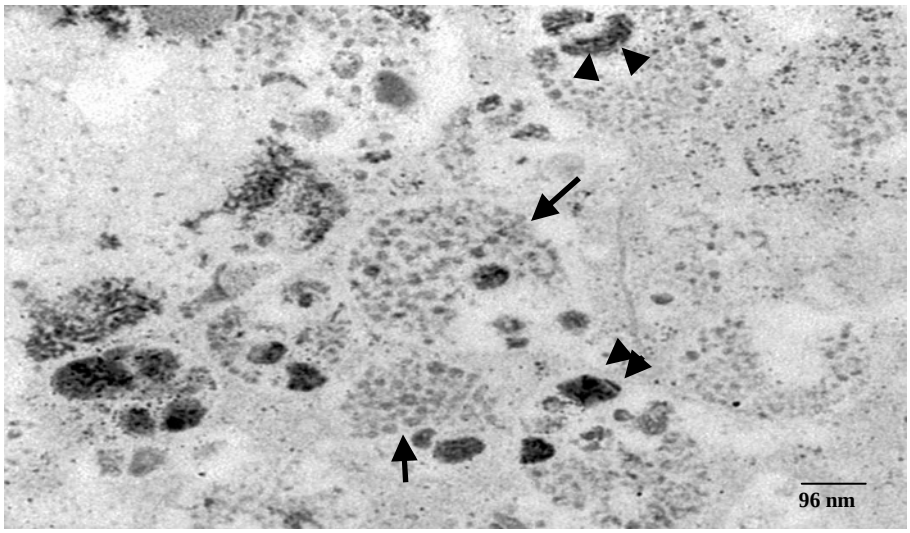

Figure 20. HBTE higher magnification TEM of exposed TLA at day 8 p.i. shows Cytoplasmic vacuoles with multiple electron-dense, well-defined circular granular bodies (arrowhead). Cytoplasmic vacuolar membrane can be distinguished with a translucent zone between the membrane and granular bodies (arrow). Particles with higher electron density are seen with the same cytoplasmic vacuoles, but are pleomorphic and restricted to the periphery of the vacuole (double arrowhead). Original magnification was used, 25000x.

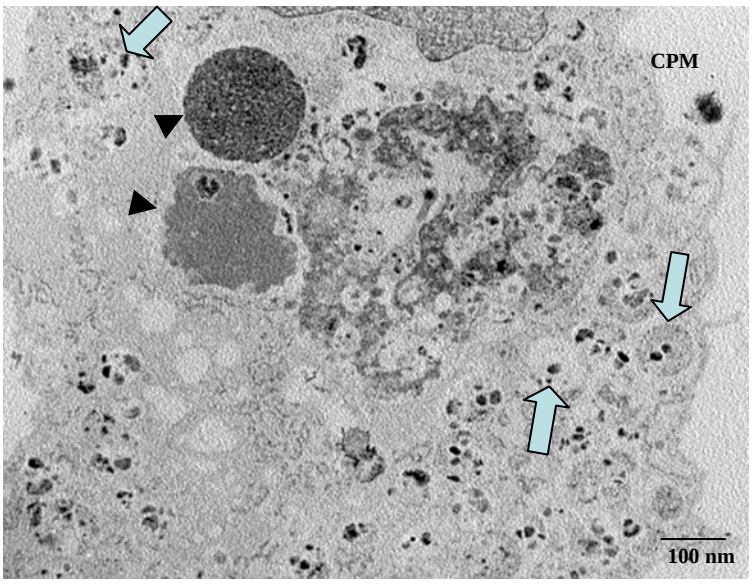

Figure 21. HBTE high magnification TEM of exposed TLA at day 10 p.i. Numerous cytoplasmic vacuoles with small pleomorphic electron-dense particles are adjacent to cell plasma membrane (CPM). In some vacuoles, the electron-dense particles are centrally located and in others they appear to lie adjacent to vacuole membrane (open arrows). Translucent vacuoles devoid of electron-dense material are centrally located within the cell. Cytoplasmic inclusion bodies are also located mid-cell (arrowheads). Original magnification was used, 75000x.

REPORT DOCUMENTATION PAGE

Form Approved
OMB No. 0704-0188

1. AGENCY USE ONLY *(Leave Blank)*	2. REPORT DATE	3. REPORT TYPE AND DATES COVERED
	June 2006	NASA Technical Paper

4. TITLE AND SUBTITLE
Three-Dimensional Human Bronchial-Tracheal Epithelial Tissue-Like Assemblies (TLAs) as Hosts For Severe Acute Respiratory Syndrome (SARS)-CoV Infection

5. FUNDING NUMBERS

6. AUTHOR(S)
Suderman, M.T.; McCarthy, M.; Mossell, E.; Watts4, D.M.; Peters, C.J.; Shope, R.; and Goodwin, T.J.

7. PERFORMING ORGANIZATION NAME(S) AND ADDRESS(ES)
Lyndon B. Johnson Space Center
Houston, Texas 77058

8. PERFORMING ORGANIZATION REPORT NUMBERS
S-980

9. SPONSORING/MONITORING AGENCY NAME(S) AND ADDRESS(ES)
National Aeronautics and Space Administration
Washington, DC 20546-0001

10. SPONSORING/MONITORING AGENCY REPORT NUMBER
TP-2006-213723

11. SUPPLEMENTARY NOTES

12a. DISTRIBUTION/AVAILABILITY STATEMENT
Available from the NASA Center for AeroSpace Information (CASI)
7121 Standard
Hanover, MD 21076-1320 Category: 51

12b. DISTRIBUTION CODE

13. ABSTRACT *(Maximum 200 words)*
A three-dimensional (3-D) tissue-like assembly (TLA) of human bronchial-tracheal mesenchymal (HBTC) cells with an overlay of human bronchial epithelial (BEAS-2B) cells was constructed using a NASA Bioreactor to survey the infectivity of SARS-CoV. This TLA was inoculated with a low passage number Urbani strain of SARS-CoV. At selected intervals over a 10-day period, media and cell aliquots of the 3-D TLA were harvested for viral titer assay and for light and electron microscopy examination. All viral titer assays were negative in both BEAS-2B two-dimensional monolayer and TLA. Light microscopy immunohistochemistry demonstrated antigen–antibody reactivity with anti-SARS-CoV polyclonal antibody to spike and nuclear proteins on cell membranes and cytoplasm. Coronavirus Group 2 cross-reactivity was demonstrated by positive reaction to anti-FIPV 1 and anti-FIPV 1 and 2 antibodies. TLA examination by transmission electron microscopy indicated increasing cytoplasmic vacuolation with numerous electron-dense bodies measuring 45 to 270 nm from days 4 through 10. There was no evidence of membrane blebbing, membrane duplication, or fragmentation of organelles in the TLAs. However, progressive disruption of endoplasmic reticulum was observed throughout the cells. Antibody response to SARS-CoV specific spike and nucleocapsid glycoproteins, cross-reactivity with FIPV antibodies, and the cytoplasmic pathology suggests this HBTE TLA model is permissive to SARS-CoV infection.

14. SUBJECT TERMS	15. NUMBER OF PAGES	16. PRICE CODE
Global positioning system, position indicators, orbit determination, space navigation, software engineering, software reliability.	40	

17. SECURITY CLASSIFICATION OF REPORT	18. SECURITY CLASSIFICATION OF THIS PAGE	19. SECURITY CLASSIFICATION OF ABSTRACT	20. LIMITATION OF ABSTRACT
Unclassified	Unclassified	Unclassified	Unlimited